

Article

# Heterojunctions of p-BiOI Nanosheets/n-TiO<sub>2</sub> Nanofibers: Preparation and Enhanced Visible-Light Photocatalytic Activity

Kexin Wang, Changlu Shao \*, Xinghua Li, Fujun Miao, Na Lu and Yichun Liu \*

Center for Advanced Optoelectronic Functional Materials Research, and Key Laboratory of UV-Emitting Materials and Technology, Northeast Normal University, Ministry of Education, 5268 Renmin Street, Changchun 130024, China; wangkx217@nenu.edu.cn (K.W.); lixh781@nenu.edu.cn (X.L.); miaofj888@nenu.edu.cn (F.M.); lun242@nenu.edu.cn (N.L.)

\* Correspondence: clshao@nenu.edu.cn (C.S.); ycliu@nenu.edu.cn (Y.L.)

Academic Editor: Joshua M. Pearce

Received: 28 December 2015; Accepted: 26 January 2016; Published: 30 January 2016

**Abstract:** p-BiOI nanosheets/n-TiO<sub>2</sub> nanofibers (p-BiOI/n-TiO<sub>2</sub> NFs) have been facilely prepared via the electrospinning technique combining successive ionic layer adsorption and reaction (SILAR). Dense BiOI nanosheets with good crystalline and width about 500 nm were uniformly assembled on TiO<sub>2</sub> nanofibers at room temperature. The amount of the heterojunctions and the specific surface area were well controlled by adjusting the SILAR cycles. Due to the synergistic effect of p-n heterojunctions and high specific surface area, the obtained p-BiOI/n-TiO<sub>2</sub> NFs exhibited enhanced visible-light photocatalytic activity. Moreover, the p-BiOI/n-TiO<sub>2</sub> NFs heterojunctions could be easily recycled without decreasing the photocatalytic activity owing to their one-dimensional nanofibrous structure. Based on the above, the heterojunctions of p-BiOI/n-TiO<sub>2</sub> NFs may be promising visible-light-driven photocatalysts for converting solar energy to chemical energy in environment remediation.

**Keywords:** BiOI/TiO<sub>2</sub>; p-n heterojunction; nanofiber; photocatalysis

## 1. Introduction

Semiconductor photocatalysts have been promising media to degrade pollutants through converting solar energy to chemical energy [1]. In recent years, bismuth oxyhalides BiOX (X = Cl, Br, I), as p-type semiconductors, have attracted considerable attentions owing to their unique layered crystal structure and indirect optical transition characteristic. The layer structure consists of (Bi<sub>2</sub>O<sub>2</sub>)<sup>2+</sup> layers interleaved by double halogen atoms layers, which can present an internal static electric field and induce the separation of photogenerated carries more efficiently. Furthermore, the indirect transition band gap is necessary for electrons to be emitted to valence band by a certain k-space distance, which reduces the recombination probability of photoelectrons and holes [2,3]. These advantages lead to remarkable photocatalytic activities in degradation of organic compounds [4–7]. Notably, the p type BiOI (p-BiOI) nanostructures have the narrowest band gap (~1.8 eV) among BiOX (X = Cl, Br, I) nanostructures. Therefore, the p-BiOI nanostructures are considered excellent visible light photocatalysts that can utilize more solar light energy in photocatalysis. Nowadays, many efforts have been employed to improve the photocatalytic efficiency of p-BiOI nanostructures [8,9]. Constructing p-n heterojunctions is considered an effective method to improve the separation efficiency of photogenerated carries due to their strong internal electric field [10–13]. Many kinds of p-n heterojunctions based on p-BiOI, such as BiOI/ZnTiO<sub>3</sub> [14], BiOI/Zn<sub>2</sub>SnO<sub>4</sub> [15], BiOI/ZnO [16], BiOI/Bi<sub>4</sub>Ti<sub>3</sub>O<sub>12</sub> [17], *etc.*, have been reported with increased photocatalytic activity.

Among many n type semiconductors, Titanium dioxide ( $\text{TiO}_2$ ) nanostructures have been widely studied as good photocatalysts due to their high efficiency, chemical stability, nontoxicity, low cost, *etc.* [18–24]. Coupling p-BiOI nanostructures with n- $\text{TiO}_2$  nanostructures to form p-BiOI/n- $\text{TiO}_2$  heterojunctions would hinder the recombination of photogenerated carries more effectively. To date, p-BiOI/n- $\text{TiO}_2$  nanoparticles have been widely reported with enhanced visible-light photocatalytic activity [25–27]. However, the suspended nanoparticles tend to aggregate during the synthesis process and be lost in the separation and recycling process, resulting in a reduction of specific surface area and photocatalytic performance. Compared with nanoparticles, one-dimensional nanofibers with a high surface-to-volume ratio are more favorable for both photocatalytic activity and recycling characteristics [28,29]. In fact, our group has previously constructed heterojunctions of p-BiOCl nanosheets/n- $\text{TiO}_2$  nanofibers [30] and p- $\text{MoO}_3$  nanosheets/n- $\text{TiO}_2$  nanofibers [31], both of which show enhanced ultraviolet photocatalytic activities and recycling properties. Therefore, there is interest in constructing p-BiOI/n- $\text{TiO}_2$  heterojunctions using electrospun  $\text{TiO}_2$  nanofibers as n type semiconductor because of the following advantages: (1) besides the internal electric field of the p-n heterojunction, the one-dimensional characters of  $\text{TiO}_2$  nanofibers could act as charge transfer channels facilitating higher charge separation efficiencies; (2) the three-dimensional open structure and large specific surface area of  $\text{TiO}_2$  nanofibers provide more active sites for the assembly of secondary nanostructures with high densities; and (3) their nanofibrous nonwoven web structure can be easily separated from fluid by sedimentation.

Taking the above factors into account, in this work, the p-type BiOI nanosheets were successfully synthesized on n-type electrospun  $\text{TiO}_2$  nanofibers by successive ionic layer adsorption and reaction (SILAR) at room temperature. The contents of BiOI in the heterojunctions of p-BiOI nanosheets/n- $\text{TiO}_2$  nanofibers (p-BiOI/n- $\text{TiO}_2$  NFs) could be well controlled by adjusting the cycles of SILAR. X-ray photoelectron spectra showed that both Ti 2p peaks of p-BiOI/n- $\text{TiO}_2$  NFs shifted to higher binding energies than that of  $\text{TiO}_2$  nanofibers, suggesting effective electrons transfer from  $\text{TiO}_2$  to BiOI in the formation of p-n heterojunction. The p-BiOI/n- $\text{TiO}_2$  NFs exhibited favorable visible-light photocatalytic activity for degradation of methyl orange (MO), which can be ascribed to the high specific surface area and the as-formed p-n heterojunctions. Moreover, the heterojunctions of p-BiOI/n- $\text{TiO}_2$  NFs could be well recycled by sedimentation without decreasing their photocatalytic activities.

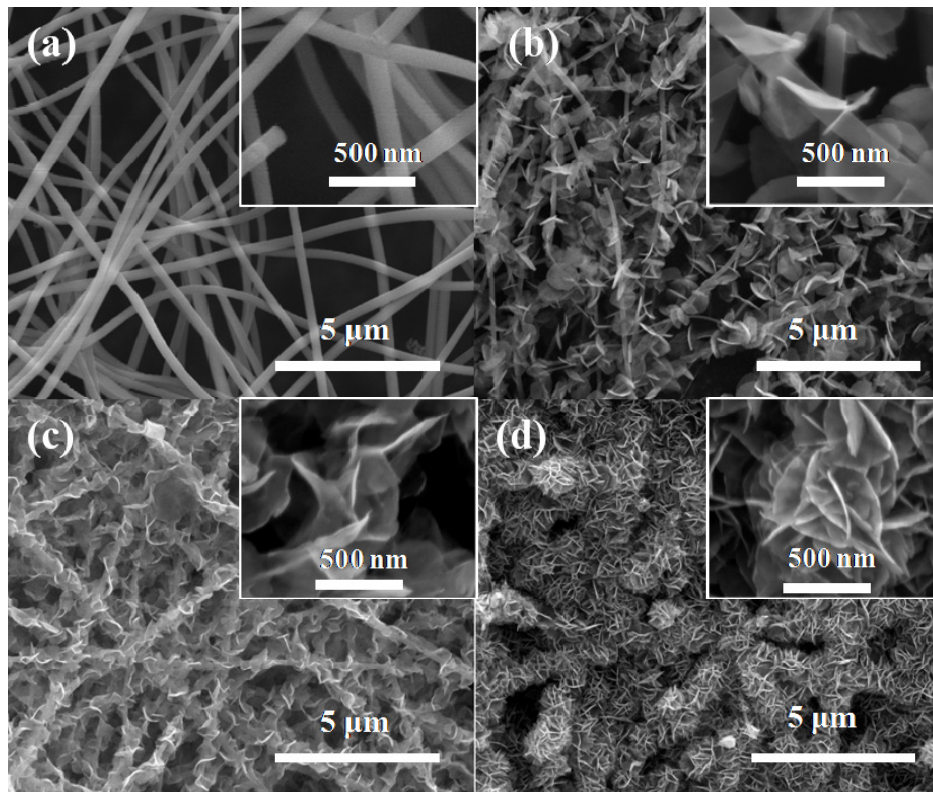
## 2. Results and Discussion

### 2.1. Morphologies

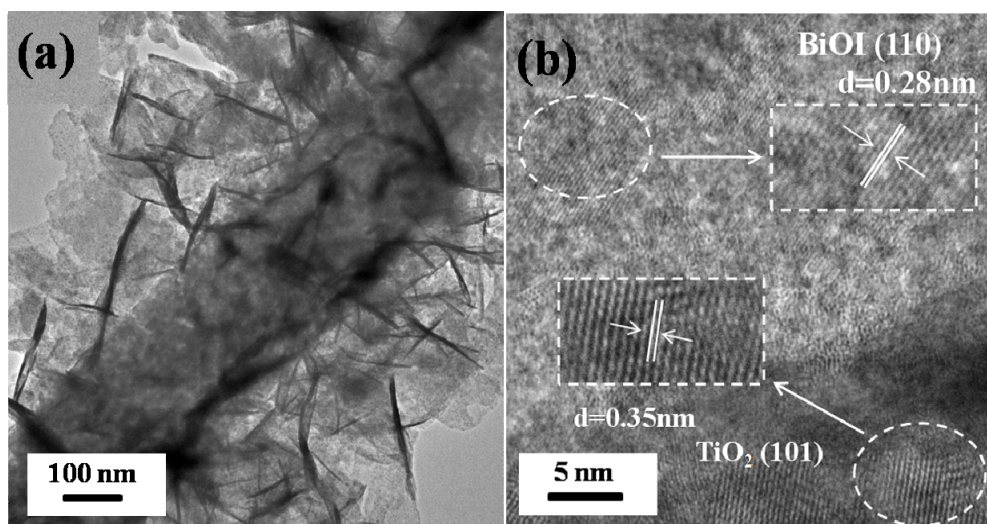
Figure 1 shows the scanning electron microscopy (SEM) images of different samples. It can be seen that  $\text{TiO}_2$  nanofibers with a diameter about 250 nm are relative smooth without secondary structures. After SILAR process, as observed in Figure 1b–d, the  $\text{TiO}_2$  nanofibers become rough and are decorated with ultrathin BiOI nanosheets and remain as one-dimension nanofibers structure. When the cycles of SILAR process increase to 30 for the BiOI/ $\text{TiO}_2$ -C30, the amount of the BiOI nanosheets increases significantly compared with those of BiOI/ $\text{TiO}_2$ -C10 and BiOI/ $\text{TiO}_2$ -C20. These results suggest that the heterojunctions of p-BiOI/n- $\text{TiO}_2$  NFs may have a higher specific surface area, which is good for the photocatalytic reactions.

Figure 2a,b shows the typical TEM images of BiOI/ $\text{TiO}_2$ -C30. It can be observed that numerous BiOI nanosheets are randomly distributed on  $\text{TiO}_2$  nanofibers. The BiOI nanosheets are very thin, which coincides with the results of SEM observations. The high-resolution transmission electron microscopy (HRTEM) image of the heterojunctions displays two types of lattice fringes, as shown in Figure 2b. One set of the fringes spacing is *ca.* 0.35 nm, corresponding to the (101) plane of the anatase crystal structure of  $\text{TiO}_2$ . Another set of the fringes spacing measures *ca.* 0.28 nm, which corresponds to the (110) lattice spacing of the BiOI. It indicates that heterojunctions are composed of  $\text{TiO}_2$  nanofibers and BiOI nanosheets with exposed {001} facets. The exposed {001} facets may have

excellent photocatalytic activity for BiOI under visible-light irradiation as reported [32]. Therefore, the surface reactivity may also be improved by decorating TiO<sub>2</sub> nanofibers with BiOI nanosheets.



**Figure 1.** (a) SEM images of TiO<sub>2</sub> nanofibers; (b) BiOI/TiO<sub>2</sub>-C10; (c) BiOI/TiO<sub>2</sub>-C20; and (d) BiOI/TiO<sub>2</sub>-C30 at low magnification and high magnification (insets).



**Figure 2.** (a) TEM; and (b) HRTEM images of BiOI/TiO<sub>2</sub>-C30.

## 2.2. Structure Characterization

Figure 3 shows the X-ray diffraction (XRD) patterns of pure TiO<sub>2</sub> nanofibers, p-BiOI/n-TiO<sub>2</sub> NFs and BiOI nanosheets. For TiO<sub>2</sub> nanofibers, all peaks are attributed to the anatase of TiO<sub>2</sub> (JCPDS No. 21-1272) and the rutile of TiO<sub>2</sub> (JCPDS No. 21-1276). For p-BiOI/n-TiO<sub>2</sub> NFs, besides the characteristic

peaks of  $\text{TiO}_2$  (solid and hollow diamonds), there are some new strong patterns that can be indexed as tetragonal phase of BiOI (JCPDS No. 73-2062). The diffraction peaks of BiOI (solid circles) are gradually intensified as the SILAR cycles increased from 0 to 30, as shown in Figure 3. No other characteristic peaks of impurities are observed. In particular, the domination of (110) plane in the pattern suggests that the exposed facets of BiOI nanosheets are mainly {001}. This result is consistent with SEM and TEM analyses.

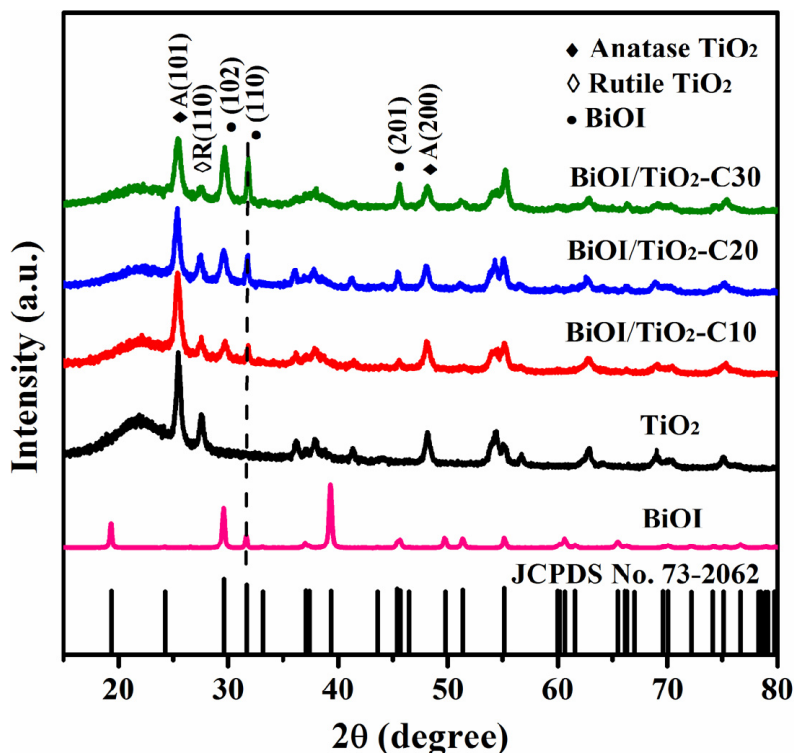
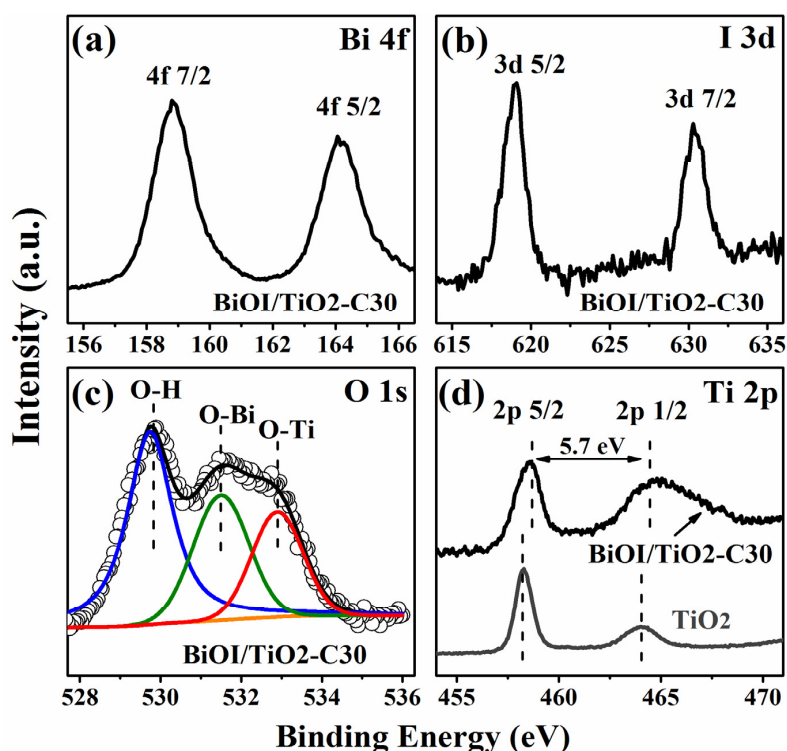


Figure 3. XRD patterns of different samples.

### 2.3. Composition and Chemical States

X-ray photoelectron spectroscopy (XPS) measurements are also performed to further investigate the chemical compositions and chemical states of p-BiOI/n- $\text{TiO}_2$  NFs. The typical high resolution XPS spectrum of Bi 4f is shown in Figure 4a. The peaks at 158.82 eV and 164.14 eV correspond to Bi 4f<sub>3/2</sub> and Bi 4f<sub>1/2</sub>, respectively, which indicates a normal state of Bi<sup>3+</sup> in BiOI/ $\text{TiO}_2$ -C30 [33]. Figure 4b reveals the high-resolution XPS spectrum of I 3d. The two peaks at 630.3 eV and 618.8 eV are attributed to I 3d<sub>3/2</sub> and I 3d<sub>5/2</sub>, respectively, which indicates that the chemical state of iodine is I<sup>-1</sup> in BiOI/ $\text{TiO}_2$ -C30 [34]. The deconvolution of the O 1s spectrum in Figure 4c implies that more than one chemical state of O 1s exists in the BiOI/ $\text{TiO}_2$ -C30. The peaks with lower binding energies at 529.8 eV and 531.5 eV correspond to the stronger Bi-O and Ti-O bond, respectively. The higher bonding energy of 532.9 eV might be caused by adsorbed water and surface hydroxyl groups (OH), which may also lead to an enhanced photocatalytic property [35]. The splitting between Ti 2p<sub>1/2</sub> and Ti 2p<sub>3/2</sub> are both 5.7 eV for  $\text{TiO}_2$  and BiOI/ $\text{TiO}_2$ -C30, suggesting a normal state of Ti<sup>4+</sup> in pure  $\text{TiO}_2$  nanofibers and BiOI/ $\text{TiO}_2$ -C30 [36,37]. However, for BiOI/ $\text{TiO}_2$ -C30, the binding energy of Ti 2p<sub>3/2</sub> locates at 458.7 eV, which is about 0.4 eV higher than that of pure  $\text{TiO}_2$  nanofibers (458.3 eV). This can be explained as follow: when p type BiOI nanosheets are deposited on n type  $\text{TiO}_2$  nanofibers, the electrons in  $\text{TiO}_2$  nanofibers would diffuse to BiOI, forming p-n heterojunctions; thus, in the space charge region,  $\text{TiO}_2$  is positively charged which could increase the binding energy of electrons in Ti 2p chemical states. Similar results have been observed in the heterojunctions of p-MoO<sub>3</sub> nanosheets/n- $\text{TiO}_2$  nanofibers [26].



**Figure 4.** (a) XPS spectra of Bi 4f; (b) I 3d; and (c) O 1s for BiOI/TiO<sub>2</sub>-C30; (d) XPS spectra of Ti 2p for TiO<sub>2</sub> nanofibers (bottom) and BiOI/TiO<sub>2</sub>-C30 (top).

#### 2.4. Nitrogen Adsorption

All the samples have typical type-IV N<sub>2</sub> adsorption-desorption isotherms with H1 hysteresis indicative of mesoporous structure (Figure 5). The curve of pure TiO<sub>2</sub> nanofibers implies a meso- and macropore structure. As we know, the precursor nanofibers of electrospun TiO<sub>2</sub> nanofibers consist of polymer and metal salt. During the calcination process, the decomposition of the polymer and metal salt can result in abundant hierarchical pores with a wide pore size distribution of more than 2 nm, as shown in Figure 5 inset. For BiOI/TiO<sub>2</sub>-C10, there is an obvious hysteresis loop in the large relative pressure range of 0.9–1.0 ( $P/P_0$ ), indicating the relatively large pore structure arising from the voids among the BiOI nanosheets on TiO<sub>2</sub> nanofibers. The specific surface areas of these samples are shown in Table 1. It is also worth noting that the BiOI/TiO<sub>2</sub>-C10 exhibit lower specific surface areas than that of TiO<sub>2</sub> nanofibers, which can be ascribed to the deposition of BiOI nanosheets blocking the original pores on TiO<sub>2</sub>. It can be clearly seen that the relative small pores (2–11 nm) are disappeared, which can be demonstrated by the pore size distribution of BiOI/TiO<sub>2</sub>-C10 in Figure 5 inset. Compared to BiOI/TiO<sub>2</sub>-C10, there is an obviously increased adsorption at high pressure with increased deposition of BiOI nanosheets on TiO<sub>2</sub> nanofibers for BiOI/TiO<sub>2</sub>-C20 and BiOI/TiO<sub>2</sub>-C30, along with increased specific surface areas, indicating the more and more abundant porosity structures. It is accepted that the porosity is relative to the amount of BiOI nanosheets depositing on TiO<sub>2</sub> nanofibers. Hence, the close arrangements of BiOI nanosheets on TiO<sub>2</sub> nanofibers (see SEM and TEM images) have resulted in the hierarchical porosity with wide pore size distributions, which are further confirmed by the corresponding pore size distributions in the inset of Figure 5. These results suggest that the BiOI/TiO<sub>2</sub> nanofibers with abundant porosity and large specific surface areas will increase the assessable surface areas of the catalyst with dye solution to achieve good photocatalytic activity. Particularly, the large amount of BiOI nanosheets depositing on TiO<sub>2</sub> nanofibers without independent nucleation will benefit the formation of more p-n heterojunctions as well as rapid charge transfer during the photocatalysis.

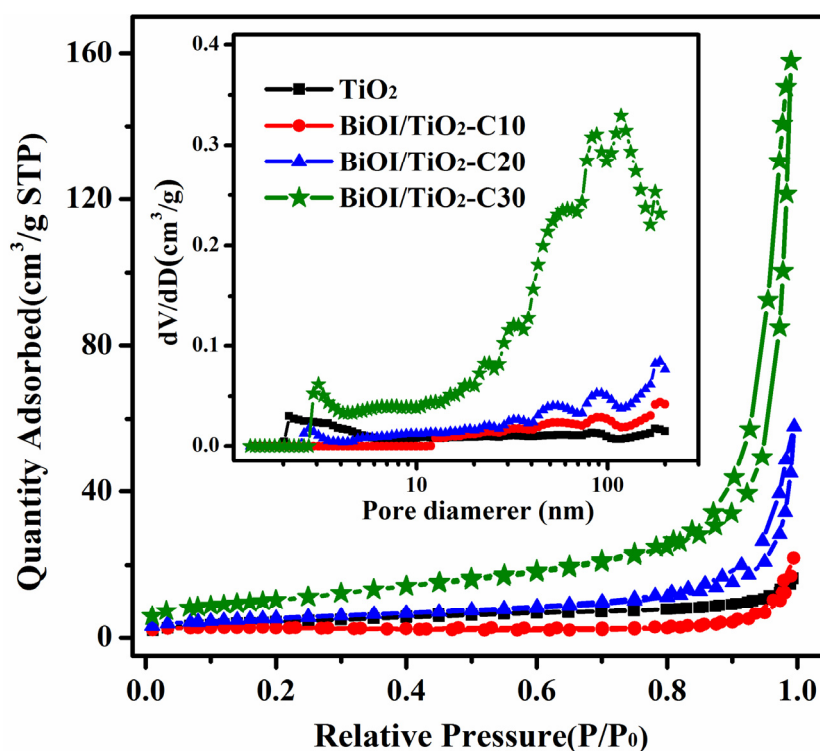


**Figure 5.** Typical N<sub>2</sub> gas adsorption-desorption isotherms of different samples and their corresponding pore-size distributions (inset).

**Table 1.** SILAR cycles, BET specific surface area and photocatalysis reaction rates of different samples.

Samples	Cycles	BET Specific Surface Area (m <sup>2</sup> /g)	K <sub>app</sub> (h <sup>-1</sup> )
TiO <sub>2</sub> NFs	0	15.88	0.000 ± 0.000
BiOI/TiO <sub>2</sub> -C10	10	7.27	0.141 ± 0.002
BiOI/TiO <sub>2</sub> -C20	20	19.19	0.197 ± 0.009
BiOI/TiO <sub>2</sub> -C30	30	38.44	0.724 ± 0.095
M-BT (Bi:Ti = 0.4:1)	-	-	0.267 ± 0.024

### 2.5. Optical Properties

Figure 6 shows the UV-vis absorption spectra of TiO<sub>2</sub>, BiOI/TiO<sub>2</sub>-C10, BiOI/TiO<sub>2</sub>-C20, BiOI/TiO<sub>2</sub>-C30 and BiOI converted from corresponding diffuse reflectance spectra by means of the Kubelka–Munk function [28]:

$$F(R) = (1 - R)^2/2R = \alpha/S \quad (1)$$

$$R = R_{Sample}/R_{BaSO4} \quad (2)$$

where  $R$ ,  $\alpha$ , and  $S$  are the reflectance, absorption coefficient and scattering coefficient, respectively. It can be seen that TiO<sub>2</sub> exhibited a typical absorption characteristic of the wide band gap semiconductor with an edge about 380 nm, while pure BiOI with a strong absorption at about 630 nm in the visible light region, indicates that it is a narrow band gap semiconductor according to the equation  $E_g = 1240/\lambda$ , where  $E_g$  is the band gap (eV) and  $\lambda$  (nm) is the wavelength of the absorption edge in the spectrum. The band gap of TiO<sub>2</sub> and BiOI are estimated to be 3.2 eV and 1.9 eV, respectively. It is noted that the absorption edge of p-BiOI/n-TiO<sub>2</sub> NFs show significant red-shift from 393 to 500 nm with the increased amount of BiOI in the composite nanofibers. Based on the above, the increased amount of BiOI in p-BiOI/n-TiO<sub>2</sub> NFs extends light absorbing range, which is the precondition of effective photocatalytic activity.

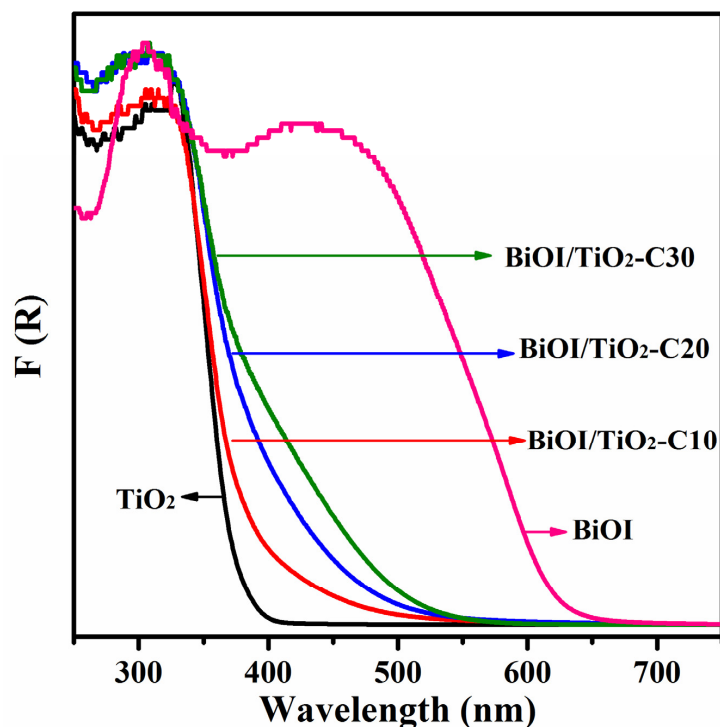


Figure 6. UV-vis absorption spectra of different samples.

## 2.6. Photocatalytic Properties

Figure 7a shows the photocatalytic activities of TiO<sub>2</sub> NFs, BiOI/TiO<sub>2</sub>-C10, BiOI/TiO<sub>2</sub>-C20, BiOI/TiO<sub>2</sub>-C30 and the mechanical mixture of BiOI and TiO<sub>2</sub> (M-BT, the molar ratio of Bi:Ti = 0.4:1 based on energy dispersive X-ray (EDX) analysis in Figure S1) on the degradation of methyl orange (MO) under visible-light irradiation ( $\geq 420$  nm). Before irradiation, the adsorption-desorption equilibrium of MO in the dark is established within 30 min over different samples. The time-dependent absorbance spectra of different samples are shown in Figure S1. The adsorption of BiOI/TiO<sub>2</sub>-C30 increases significantly compared to other samples, which might be attributed to the high specific surface area. After 3 h irradiation, the photodegradation efficiencies of MO for BiOI/TiO<sub>2</sub>-C30 are about 92%, in comparison to 60%, 66%, 38% and almost none for M-BT, BiOI/TiO<sub>2</sub>-C20, BiOI/TiO<sub>2</sub>-C10 and TiO<sub>2</sub> nanofibers, respectively. In Figure 7b, the kinetic linear fitting curves over different photocatalysts show that the photocatalytic degradation of MO followed a Langmuir-Hinshelwood apparent first-order kinetics model:

$$\ln C/C_0 = -kKt = -k_{app}t \quad (3)$$

where  $C_0$  is the initial concentration (mg/L) of the reactant;  $C$  is the concentration (mg/L);  $t$  is the visible-light irradiation time;  $k$  is the reaction rate constant (mg/(L·min)); and  $K$  is the adsorption coefficient of the reactant (L/mg);  $k_{app}$  is the apparent first-order rate constant ( $\text{min}^{-1}$ ). The  $k_{app}$  of different samples are shown in Table 1. It is indicated that the photocatalytic activities is in the order of BiOI/TiO<sub>2</sub>-C30 > BiOI/TiO<sub>2</sub>-C20 > M-BT > BiOI/TiO<sub>2</sub>-C10 > TiO<sub>2</sub>. The above illuminates that the construction of p-n heterojunctions can effectively enhance the photocatalytic properties. Furthermore, the increased of the specific surface area and the amount of p-n heterojunctions obviously enhance the photocatalytic activity. Furthermore, the photocatalysis under UV-light irradiation (Figure S2) also demonstrates the above point.

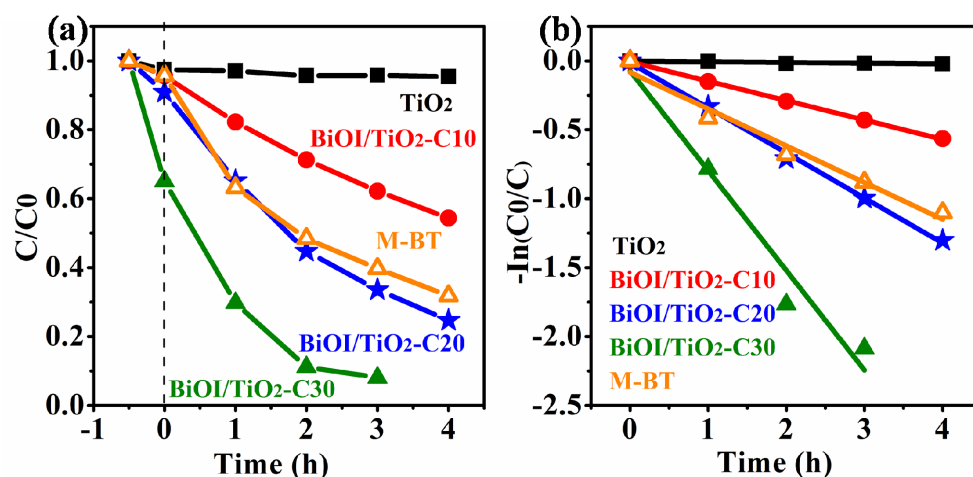
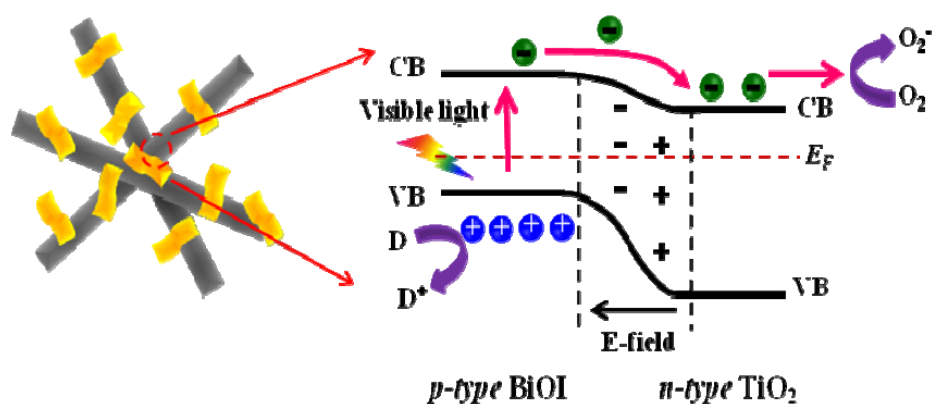


**Figure 7.** (a) Degradation curves of MO under visible light irradiation; and (b) the apparent first-order kinetics fitting over different samples.

To understand the photocatalytic properties of p-BiOI/n-TiO<sub>2</sub> NFs, a schematic diagram is proposed (Scheme 1). When p-type BiOI contacts n-type TiO<sub>2</sub>, the diffusion of electrons and holes create an inner electric field where a space-charge region is formed at the interfaces of p-n heterojunction. Under visible-light irradiation, the photogenerated electrons transfer from the conduction band of BiOI to that of TiO<sub>2</sub>, while the photogenerated holes stay at the valence band of BiOI. The recombination of photogenerated charge carrier is inhibited greatly in the heterojunctions of p-BiOI/n-TiO<sub>2</sub> NFs. Thus, the photogenerated electrons and holes can effectively take part in the photodegradation of MO under visible light. On the other hand, the nanofiber structures of TiO<sub>2</sub> can prevent the agglomeration of BiOI nanosheets and facilitate the transfer of the dye molecules during photocatalytic process. Moreover, the exposed surface of BiOI is mainly {001} facet, which is very active for photocatalytic reactions under visible-light irradiation [32]. Thus, the nanosheet structure of BiOI might also improve the surface reaction rates and contribute to the photocatalysis. It should be noted that the p-BiOI/n-TiO<sub>2</sub> NFs can be easily separated from an aqueous suspension for reuse due to their one-dimensional nanofibrous morphology. As shown in Figure 8, the photodegradation of MO on the p-BiOI/n-TiO<sub>2</sub> NFs was reused three times. Each experiment was carried out under identical conditions. Clearly, the photocatalytic activity of p-BiOI/n-TiO<sub>2</sub> NFs remains almost unchanged after three-cycles, suggesting that the BiOI/TiO<sub>2</sub> NFs have good stability and recycling properties.



**Scheme 1.** Possible photocatalytic reactions of p-BiOI/n-TiO<sub>2</sub> NFs heterojunctions.

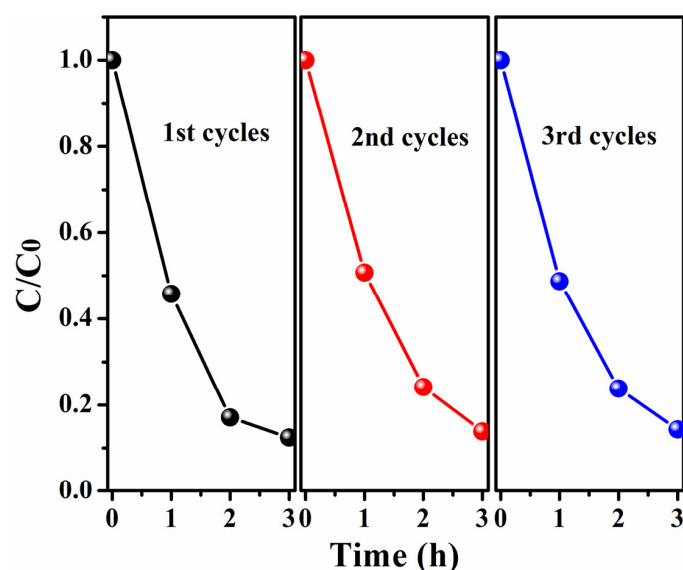
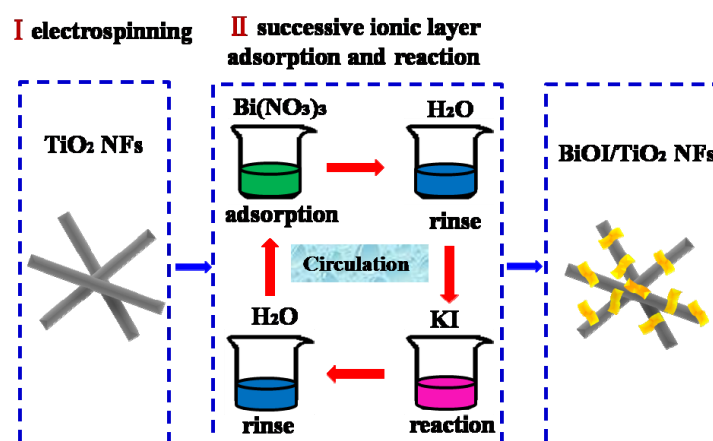


Figure 8. Photocatalysis tests of BiOI/TiO<sub>2</sub>-C30 for three cycles.

### 3. Experimental

The synthesized process of samples is presented in Scheme 2.



Scheme 2. Schematic illustration for the preparation of p-BiOI/n-TiO<sub>2</sub> NFs heterojunctions.

#### 3.1. Fabrication of TiO<sub>2</sub> Nanofibers

Firstly, 1.6 g Poly(vinyl pyrrolidone) powder (PVP, Mw = 1,300,000) was added to a mixture of 20 mL absolute ethanol and 2 mL acetic acid in a Erlenmeyer flask. The obtained solution was stirred for 2 h to generate a homogeneous solution. Then, 2.0 mL Ti(OC<sub>4</sub>H<sub>9</sub>)<sub>4</sub> was added to the solution, the mixture was magnetically stirred for another 10 h at room temperature to make electrospinning precursor solution. Subsequently, the above precursor solutions were drawn into a hypodermic syringe with a needle tip. Then, a high voltage source was connected to the needle tip while a sheet of aluminum foil was employed as the collector. The voltage between the needle tip and collector was set at 10 kV, and the distance was 15 cm. The as-collected nanofibers were calcined at a rate of 25 °C/h and remained for 2 h at 520 °C to obtain TiO<sub>2</sub> NFs.

### 3.2. Fabrication of BiOI/TiO<sub>2</sub> Nanofibers

The p-BiOI/n-TiO<sub>2</sub> NFs were synthesized through the SILAR process. Typically, 0.25 mM Bi(NO<sub>3</sub>)<sub>3</sub>·5H<sub>2</sub>O solutions were prepared with deionized water as solution A, and equivalent concentration of KI solution were prepared as solution B. The TiO<sub>2</sub> nanofibers were first immersed into solution A for 2 min, rinsed with deionized water, and then immersed into solution B for 2 min, rinsing likewise. The four-step procedure forms one cycle and the BiOI would increase by repeating the cycles. A series of samples, with different cycles of 10, 20 and 30 were prepared and denoted as BiOI/TiO<sub>2</sub>-C10, BiOI/TiO<sub>2</sub>-C20 and BiOI/TiO<sub>2</sub>-C30. After that, the samples were thoroughly rinsed with deionized water and allowed to dry at 60 °C overnight. All the samples are listed in Table 1. Pure BiOI nanosheets were prepared by mixing solution A and B, then rinsed and dried.

### 3.3. Characterizations

Scanning electron microscopy (SEM, Quanta 250 FEG, FEI, Hillsboro, OR, USA) and high-resolution transmission electron microscopy (HRTEM; JEOL JEM-2100, JEOL, Tokyo, Japan) were used to characterize the morphologies of the products. The X-ray diffraction (XRD) measurements were carried out using a D/max 2500 XRD spectrometer (Rigaku, Tokyo, Japan) with a Cu K $\alpha$  line of 0.1541 nm. The X-ray photoelectron spectroscopy (XPS) was performed on a VG-ESCALAB LKII instrument (VG, Waltham, UK) with Mg K $\alpha$  ADES ( $h\nu = 1253.6$  eV) source at a residual gas pressure of below  $10^{-8}$  Pa. The specific surface area of the samples were measured with a Micromeritics ASAP 2010 instrument (Micromeritics, Norcross, GA, USA) and analyzed by the Brunauer-Emmett-Teller (BET) method. The UV-vis diffuse reflectance spectra were measured at room temperature with a UH4150 spectrophotometer (Hitachi, Tokyo, Japan).

### 3.4. Photocatalytic Tests

A 150 W xenon lamp with a cut off filter ( $\geq 420$  nm) was used as the visible light source for photocatalysis. Using MO as model pollutants, photocatalyst (0.1 g) was suspended in MO solution (100 mL, 10 mg/L) with stirring. The solution was kept in the dark for 30 min to reach adsorption-desorption equilibrium between the organic molecules and the photocatalyst surface. Then, 4 mL reacted solutions in series were taken out and analyzed every 1 h. The concentrations of MO in the reacting solutions were analyzed by a Cary 500 UV-vis-NIR spectrophotometer (Varian, Palo Alto, CA, USA) at 464 nm.

## 4. Conclusions

In summary, using electrospinning technology and SILAR method, heterojunctions of p-BiOI/n-TiO<sub>2</sub> NFs have been successfully fabricated. Due to the p-n heterojunction effects and large specific surface area, the BiOI/TiO<sub>2</sub>-C30 exhibits higher visible-light photocatalytic behavior in comparison with other samples for degradation of MO. Furthermore, the p-BiOI/n-TiO<sub>2</sub> NFs can be easily recycled without a decrease of the photocatalytic activity because of their nanofibrous nonwoven web structure property. It is expected that the p-BiOI/n-TiO<sub>2</sub> NFs with high photocatalytic activity will greatly promote their industrial application to eliminate the organic and inorganic pollutants from wastewater.

**Supplementary Materials:** The following are available online at [www.mdpi.com/1996-1944/9/2/90/s1](http://www.mdpi.com/1996-1944/9/2/90/s1).

**Acknowledgments:** The work is supported financially by the National Basic Research Program of China (973 Program) (Grant No. 2012CB933703), the National Natural Science Foundation of China (No. 91233204, 51272041, 61201107, and 51572045), the 111 Project (No. B13013), and the Fundamental Research Funds for the Central Universities (12SSXM001).

**Author Contributions:** Kexin Wang and Xinghua Li performed the experiments and analyzed the data; Changlu Shao and Yichun Liu designed the experiments and revised the draft; Na Lu and Fujun Miao contribute reagents/materials/analysis tools; and Kexin Wang wrote the paper.

**Conflicts of Interest:** The authors declare no conflict of interest.

## References

1. Hoffmann, M.R.; Martin, S.T.; Choi, W.; Bahnemann, D.W. Environmental applications of semiconductor photocatalysis. *Chem. Rev.* **1995**, *95*, 69–96. [[CrossRef](#)]
2. Zhang, K.; Liu, C.; Huang, F.; Zheng, C.; Wang, W. Study of the electronic structure and photocatalytic activity of the BiOCl photocatalyst. *Appl. Catal. B Environ.* **2006**, *68*, 125–129. [[CrossRef](#)]
3. Zhang, X.; Liu, X.; Fan, C.; Wang, Y.; Wang, Y.; Liang, Z. A novel BiOCl thin film prepared by electrochemical method and its application in photocatalysis. *Appl. Catal. B Environ.* **2013**, *132–133*, 332–341. [[CrossRef](#)]
4. Zhang, X.; Ai, Z.H.; Jia, F.L.; Zhang, L.Z. Generalized one-pot synthesis, characterization, and photocatalytic activity of hierarchical BiOX (X = Cl, Br, I) nanoplate microspheres. *J. Phys. Chem. C* **2008**, *112*, 747–753. [[CrossRef](#)]
5. Wang, D.H.; Gao, G.Q.; Zhang, Y.W.; Zhou, L.S.; Xu, A.W.; Chen, W. Nanosheet-constructed porous BiOCl with dominant {001} facets for superior photosensitized degradation. *Nanoscale* **2012**, *4*, 7780–7785. [[CrossRef](#)] [[PubMed](#)]
6. Huo, Y.; Zhang, J.; Miao, M.; Jin, Y. Solvothermal synthesis of flower-like BiOBr microspheres with highly visible-light photocatalytic performances. *Appl. Catal. B Environ.* **2012**, *111–112*, 334–341. [[CrossRef](#)]
7. Ye, L.Q.; Chen, J.N.; Tian, L.H.; Liu, J.Y.; Peng, T.Y.; Deng, K.J.; Zan, L. BiOI thin film via chemical vapor transport: Photocatalytic activity, durability, selectivity and mechanism. *Appl. Catal. B Environ.* **2013**, *130*, 1–7. [[CrossRef](#)]
8. Cheng, H.; Wang, W.; Huang, B.; Wang, Z.; Zhan, J.; Qin, X.; Zhang, X.; Dai, Y. Tailoring AgI nanoparticles for the assembly of AgI/BiOI hierarchical hybrids with size-dependent photocatalytic activities. *J. Mater. Chem. A* **2013**, *1*, 7131–7136. [[CrossRef](#)]
9. Xiao, X.; Zhang, W.-D. Facile synthesis of nanostructured BiOI microspheres with high visible light-induced photocatalytic activity. *J. Mater. Chem.* **2010**, *20*, 5866–5870. [[CrossRef](#)]
10. Cao, S.; Chen, C.; Liu, T.; Tsang, Y.; Zhang, X.; Yu, W.; Chen, W. Synthesis of reduced graphene oxide/ $\alpha$ -Bi<sub>2</sub>Mo<sub>3</sub>O<sub>12</sub>@ $\beta$ -Bi<sub>2</sub>O<sub>3</sub> heterojunctions by organic electrolytes assisted UV-excited method. *Chem. Eng. J.* **2014**, *257*, 309–316. [[CrossRef](#)]
11. Peng, Y.; Yan, M.; Chen, Q.G.; Fan, C.M.; Zhou, H.Y.; Xu, A.W. Novel onedimensional Bi<sub>2</sub>O<sub>3</sub>-Bi<sub>2</sub>WO<sub>6</sub> p-n hierarchical heterojunction with enhanced photocatalytic activity. *J. Mater. Chem. A* **2014**, *2*, 8517–8524. [[CrossRef](#)]
12. Chang, X.X.; Wang, T.; Zhang, P.; Zhang, J.J.; Li, A.; Gong, J.L. Enhanced surface reaction kinetics and charge separation of p-n heterojunction Co<sub>3</sub>O<sub>4</sub>/BiVO<sub>4</sub> photoanodes. *J. Am. Chem. Soc.* **2015**, *137*, 8356–8359. [[CrossRef](#)] [[PubMed](#)]
13. Liu, Y.; Zhang, M.; Li, L.; Zhang, X. One-dimensional visible-light-driven bifunctional photocatalysts based on Bi<sub>4</sub>Ti<sub>3</sub>O<sub>12</sub> nanofiber frameworks and Bi<sub>2</sub>XO<sub>6</sub> (X=Mo, W) nanosheets. *Appl. Catal. B Environ.* **2014**, *160–161*, 757–766. [[CrossRef](#)]
14. Reddy, K.H.; Martha, S.; Parida, K.M. Fabrication of novel p-BiOI/n-ZnTiO<sub>3</sub> heterojunction for degradation of rhodamine 6G under visible light irradiation. *Inorg. Chem.* **2013**, *52*, 6390–6401. [[CrossRef](#)] [[PubMed](#)]
15. Li, H.; Jin, Z.; Sun, H.; Sun, L.; Li, Q.; Zhao, X.; Jia, C.-J.; Fan, W. Facile fabrication of p-BiOI/n-Zn<sub>2</sub>SnO<sub>4</sub> heterostructures with highly enhanced visible light photocatalytic performances. *Mater. Res. Bull.* **2014**, *55*, 196–204. [[CrossRef](#)]
16. Jiang, J.; Zhang, X.; Sun, P.; Zhang, L. ZnO/BiOI heterostructures: Photoinduced charge-transfer property and enhanced visible-light photocatalytic activity. *J. Phys. Chem. C* **2011**, *115*, 20555–20564. [[CrossRef](#)]
17. Hou, D.; Hu, X.; Hu, P.; Zhang, W.; Zhang, M.; Huang, Y. Bi<sub>4</sub>Ti<sub>3</sub>O<sub>12</sub> nanofibers-BiOI nanosheets p-n junction: Facile synthesis and enhanced visible-light photocatalytic activity. *Nanoscale* **2013**, *5*, 9764–9772. [[CrossRef](#)] [[PubMed](#)]
18. Yoneyama, H.; Yamashita, Y.; Tamura, H. Heterogeneous photocatalytic reduction of dichromate on n-type semiconductor catalysts. *Nature* **1979**, *282*, 817–818. [[CrossRef](#)]
19. Schneider, J.; Matsuoka, M.; Takeuchi, M.; Zhang, J.L.; Horiuchi, Y.; Anpo, M.; Bahnemann, D.W. Understanding TiO<sub>2</sub> photocatalysis: Mechanisms and materials. *Chem. Rev.* **2014**, *114*, 9919–9986. [[CrossRef](#)] [[PubMed](#)]

20. Liu, M.; Li, H.; Zeng, Y.; Huang, T. Anatase TiO<sub>2</sub> single crystals with dominant {001} facets: Facile fabrication from Ti powders and enhanced photocatalytic activity. *Appl. Surf. Sci.* **2013**, *274*, 117–123. [[CrossRef](#)]
21. Liu, M.; Piao, L.; Ju, S.; Lu, W.; Zhao, L.; Zhou, C.; Wang, W. Fabrication of micrometer-scale spherical titanate nanotube assemblies with high specific surface area. *Mater. Lett.* **2010**, *64*, 1204–1207. [[CrossRef](#)]
22. Liu, M.; Zhong, M.; Li, H.; Piao, L.; Wang, W. Facile synthesis of hollow TiO<sub>2</sub> single nanocrystals with improved photocatalytic and photoelectrochemical activities. *ChemPlusChem* **2015**, *80*, 688–696. [[CrossRef](#)]
23. Liu, M.; Piao, L.; Wang, W. Hierarchical TiO<sub>2</sub> spheres: Facile fabrication and enhanced photocatalysis. *Rare Metals* **2011**, *30*, 153–156. [[CrossRef](#)]
24. Liu, M.; Sunada, K.; Hashimoto, K.; Miyauchi, M. Visible-light sensitive Cu(ii)-TiO<sub>2</sub> with sustained anti-viral activity for efficient indoor environmental remediation. *J. Mater. Chem. A* **2015**, *3*, 17312–17319. [[CrossRef](#)]
25. Wu, D.Y.; Wang, H.Y.; Li, C.L.; Xia, J.; Song, X.J.; Huang, W.S. Photocatalytic self-cleaning properties of cotton fabrics functionalized with p-BiOI/n-TiO<sub>2</sub> heterojunction. *Surf. Coat. Technol.* **2014**, *258*, 672–676. [[CrossRef](#)]
26. Li, Y.; Wang, J.; Liu, B.; Dang, L.; Yao, H.; Li, Z. BiOI-sensitized TiO<sub>2</sub> in phenol degradation: A novel efficient semiconductor sensitizer. *Chem. Phys. Lett.* **2011**, *508*, 102–106. [[CrossRef](#)]
27. Zhang, D. Heterostructural BiOI/TiO<sub>2</sub> composite with highly enhanced visible light photocatalytic performance. *Russ. J. Phys. Chem. A* **2014**, *88*, 2476–2485. [[CrossRef](#)]
28. Zhang, Z.; Shao, C.; Li, X.; Sun, Y.; Zhang, M.; Mu, J.; Zhang, P.; Guo, Z.; Liu, Y. Hierarchical assembly of ultrathin hexagonal SnS<sub>2</sub> nanosheets onto electrospun TiO<sub>2</sub> nanofibers: Enhanced photocatalytic activity based on photoinduced interfacial charge transfer. *Nanoscale* **2013**, *5*, 606–618. [[CrossRef](#)] [[PubMed](#)]
29. Liu, C.; Wang, L.; Tang, Y.; Luo, S.; Liu, Y.; Zhang, S.; Zeng, Y.; Xu, Y. Vertical single or few-layer MoS<sub>2</sub> nanosheets rooting into TiO<sub>2</sub> nanofibers for highly efficient photocatalytic hydrogen evolution. *Appl. Catal. B Environ.* **2015**, *164*, 1–9. [[CrossRef](#)]
30. Wang, K.X.; Shao, C.L.; Li, X.H.; Zhang, X.; Lu, N.; Miao, F.J.; Liu, Y.C. Hierarchical heterostructures of p-type BiOCl nanosheets on electrospun n-type TiO<sub>2</sub> nanofibers with enhanced photocatalytic activity. *Catal. Commun.* **2015**, *67*, 6–10. [[CrossRef](#)]
31. Lu, M.X.; Shao, C.L.; Wang, K.X.; Lu, N.; Zhang, X.; Zhang, P.; Zhang, M.Y.; Li, X.H.; Liu, Y.C. p-MoO<sub>3</sub> nanostructures/n-TiO<sub>2</sub> nanofiber heterojunctions: Controlled fabrication and enhanced photocatalytic properties. *ACS Appl. Mater. Inter.* **2014**, *6*, 9004–9012. [[CrossRef](#)] [[PubMed](#)]
32. Ye, L.; Tian, L.; Peng, T.; Zan, L. Synthesis of highly symmetrical BiOI single-crystal nanosheets and their {001} facet-dependent photoactivity. *J. Mater. Chem.* **2011**, *21*, 12479–12484. [[CrossRef](#)]
33. Wang, S.M.; Guan, Y.; Wang, L.P.; Zhao, W.; He, H.; Xiao, J.; Yang, S.G.; Sun, C. Fabrication of a novel bifunctional material of BiOI/Ag<sub>3</sub>VO<sub>4</sub> with high adsorption-photocatalysis for efficient treatment of dye wastewater. *Appl. Catal. B Environ.* **2015**, *168*, 448–457. [[CrossRef](#)]
34. Liu, H.; Cao, W.; Su, Y.; Wang, Y.; Wang, X. Synthesis, characterization and photocatalytic performance of novel visible-light-induced Ag/BiOI. *Appl. Catal. B Environ.* **2012**, *111–112*, 271–279. [[CrossRef](#)]
35. Chu, M.-W.; Ganne, M.; Caldes, M.T.; Brohan, L. X-ray photoelectron spectroscopy and high resolution electron microscopy studies of Aurivillius compounds: Bi<sub>4-x</sub>La<sub>x</sub>Ti<sub>3</sub>O<sub>12</sub> (x = 0, 0.5, 0.75, 1.0, 1.5, and 2.0). *J. Appl. Phys.* **2002**, *91*, 3178. [[CrossRef](#)]
36. Wei, X.X.; Chen, C.M.; Guo, S.Q.; Guo, F.; Li, X.M.; Wang, X.X.; Cui, H.T.; Zhao, L.F.; Li, W. Advanced visible-light-driven photocatalyst BiOBr-TiO<sub>2</sub>-graphene composite with graphene as a nano-filler. *J. Mater. Chem. A* **2014**, *2*, 4667–4675. [[CrossRef](#)]
37. Zhang, Y.C.; Yang, M.; Zhang, G.S.; Dionysiou, D.D. HNO<sub>3</sub>-involved one-step low temperature solvothermal synthesis of N-doped TiO<sub>2</sub> nanocrystals for efficient photocatalytic reduction of Cr(VI) in water. *Appl. Catal. B Environ.* **2013**, *142*, 249–258. [[CrossRef](#)]

